Rare Metal Materials and Engineering
Volume 55, Issue 2, Feburary 2026
Available online at www.rmme.ac.cn

Science Press

Cite this article as: Lu Durui, Song Suocheng, Lu Bingheng. Research Progress on Process Optimization and Performance Control of Additive Manufacturing for Refractory Metals[J]. Rare Metal Materials and Engineering, 2026, 55(02): 345-364. DOI: https://doi.org/10.12442/j.issn.1002-185X.20250370.

REVIEW

Research Progress on Process Optimization and Performance Control of Additive Manufacturing for Refractory Metals

Lu Durui[1], Song Suocheng[1], Lu Bingheng[2,3]

[1] State Key Laboratory for Mechanical Behavior of Materials, Xi'an Jiaotong University, Xi'an 710049, China; [2] National Innovation Institute of Additive Manufacturing, Xi'an 710300, China; [3] School of Mechanical Engineering, Xi'an Jiaotong University, Xi'an 710049, China

Abstract: Refractory metals, including tungsten (W), tantalum (Ta), molybdenum (Mo), and niobium (Nb), play a vital role in industries, such as nuclear energy and aerospace, owing to their exceptional melting temperatures, thermal durability, and corrosion resistance. These metals have body-centered cubic crystal structure, characterized by limited slip systems and impeded dislocation motion, resulting in significant low-temperature brittleness, which poses challenges for the conventional processing. Additive manufacturing technique provides an innovative approach, enabling the production of intricate parts without molds, which significantly improves the efficiency of material usage. This review provides a comprehensive overview of the advancements in additive manufacturing techniques for the production of refractory metals, such as W, Ta, Mo, and Nb, particularly the laser powder bed fusion. In this review, the influence mechanisms of key process parameters (laser power, scan strategy, and powder characteristics) on the evolution of material microstructure, the formation of metallurgical defects, and mechanical properties were discussed. Generally, optimizing powder characteristics, such as sphericity, implementing substrate preheating, and formulating alloying strategies can significantly improve the densification and crack resistance of manufactured parts. Meanwhile, strictly controlling the oxygen impurity content and optimizing the energy density input are also the key factors to achieve the simultaneous improvement in strength and ductility of refractory metals. Although additive manufacturing technique provides an innovative solution for processing refractory metals, critical issues, such as residual stress control, microstructure and performance anisotropy, and process stability, still need to be addressed. This review not only provides a theoretical basis for the additive manufacturing of high-performance refractory metals, but also proposes forward-looking directions for their industrial application.

Key words: refractory metals; additive manufacturing; mechanical properties; microstructure evolution; optimization of printing process

1 Introduction

With the breakthrough demands from technological fields, such as nuclear reactors, aerospace propulsion systems, and hypersonic vehicles, for extremely high-temperature environments, the maximum service temperatures of traditional superalloys gradually cannot meet the application requirements. Against this backdrop, refractory metals, represented by tungsten (W), tantalum (Ta), molybdenum (Mo), niobium (Nb), and rhenium (Re) with melting points generally exceeding 2000 °C, have garnered attention owing to their unique body-centered cubic (bcc)/hexagonal close packed (hcp) crystal structures and excellent properties[1–3]. These materials are primarily distinguished by their outstanding wear resistance and high interfacial stability, which is attributed to the inherent physical characteristics, including exceptional strength at elevated temperatures, ultra-high density, and minimal thermal expansion coefficient[2,4–6]. Consequently, the refractory metals play an irreplaceable and critical role in extreme operating conditions, including radioactive environments, spacecraft thermal protection, and nuclear fuel cladding[7–9]. However, although the

Received date: July 17, 2025
Foundation item: National MCF Energy R&D Program (2024YFE03260300)
Corresponding author: Song Suocheng, Ph. D., Associate Professor, State Key Laboratory for Mechanical Behavior of Materials, Xi'an Jiaotong University, Xi'an 710049, P. R. China, E-mail: scsong1989@xjtu.edu.cn; Lu Bingheng, Ph. D., Professor, National Innovation Institute of Additive Manufacturing, Xi'an 710300, P. R. China, E-mail: bhlu@xjtu.edu.cn

comprehensive properties of these metals can be further enhanced through alloying method, such as Cu-Mo-Si system[10] and Ti-Zr-Nb system[11], bottlenecks in processing technology significantly constrain their industrial application. The mechanical and chemical properties of refractory metals severely restrict the applicability of traditional casting and forging of these base materials. Technically, their ultra-high yield strength (YS) coupled with low-temperature brittleness resists the plastic deformation, but their susceptibility to oxidation compromises with the material integrity during high-temperature processing, thus precluding the precise fabrication of complex components[12]. These issues propose higher requirements for the fabrication technologies, particularly for the additive manufacturing (AM) techniques.

Refractory metals, such as W, Ta, Mo, and Nb, play a crucial role in high-temperature applications and special environments. As shown in Fig.1[13–14], the main applications of refractory metals are primarily concentrated in aerospace, aviation, biomedical implants, and nuclear applications. Among these refractory metals, W with melting point of 3422 °C presents the most excellent high-temperature performance, which is also the upper thermal limit for all metallic materials[1]. The melting point of Re is the second highest of 3182 °C, but Re has the highest density of 21 g/cm^3[15–20]. In contrast, Nb has the lowest melting point (2477 °C) and density (8.75 g/cm^3) among these materials[1]. A critical performance difference lies in their mechanical behavior, particularly the ductility and brittleness at room temperature. The high ductile-to-brittle transition temperature (DBTT) of W is over 300 °C and DBTT range of Mo is 0–50 °C. Thus, both W and Mo metals are prone to brittle fracture, posing significant processing challenges[15,18]. Conversely, Ta and Nb exhibit excellent ductility. This desirable characteristic is related to their ability to form stable protective oxide layers, which also

Fig.1 Typical applications of AM-prepared refractory metals[13–14]

grants them outstanding corrosion resistance[18–19]. Superior chemical inertness is also a key factor to the applications. Ta is a unique versatile metal, valued in disparate demanding fields. Its exceptional biocompatibility and corrosion resistance make it a leading material for medical implants and valves. Concurrently, its chemical inertness and high-temperature stability (melting point of 3020 ° C) render it highly suitable for constructing robust heat exchangers in corrosive chemical environments[16–18]. Nb has fine stability against various acids and it is usually used for superconductors in the chemical and medical industries[18–19]. The most common application for refractory metals is potent alloying agents. The high strength and good ductility characteristics of Re make it specifically used to strengthen the superalloys[20–25]. Likewise, Mo and Nb are crucial additives to strengthen the steels and superalloys. Even a minor amount of Nb can yield dramatic improvements in strength[1,18]. Additionally, these refractory metals provide critical functions in extreme environments. For instance, W is vital for hypersonic aircraft due to its exceptional high-temperature properties. Concurrently, its robust radiation resistance makes it suitable for plasma-facing reactor components. Furthermore, W carbide, owing to its ultra-high hardness, is extensively used in the production of superhard cutting tools[1,15].

AM technique offers significant technical advantages in the processing of refractory metals, and it is particularly suitable for the low-volume production of customized components with complex geometric features. Compared with conventional manufacturing processes, this layer-by-layer fabrication method can improve the material utilization to over 90%, significantly reducing the processing loss of high-cost refractory metals[26–28]. From the perspective of microstructure control, the rapid melting and solidification process unique to AM can yield fine-grained microstructures with grain sizes at the micrometer or even sub-micrometer scale. In this microscopic structure, the high-density grain boundaries effectively impede the movement of dislocations. According to the Hall-Petch relationship, YS and hardness of the material can be significantly improved after grain refinement. More significantly, by accurately adjusting the process parameters, it is possible to construct a controlled dislocation network. This approach not only enhances the material strength but also preserves the ability for plastic deformation, thus breaking through the strength-ductility contradiction of metallic materials[29].

Currently, the primary AM techniques employed for refractory metals are mainly laser powder bed fusion (L-PBF), laser directed energy deposition (L-DED), and electron beam powder bed fusion (EB-PBF). Although both L-PBF and L-DED use the laser energy source, their process characteristics differ significantly. L-PBF is suitable for fabricating fine complex structures and features higher cooling rates, which can produce finer microstructures but may also lead to higher residual stresses[7,30–31]. In contrast, L-DED employs a synchronous powder feeding method, making it more suitable for manufacturing large parts with

faster production speed and supporting the multi-material fabrication. However, the surface roughness is relatively poor after L-DED process[32–34]. The EB-PBF process is unique due to its high-vacuum preparation environment and adjustable preheating temperature range, which effectively reduce impurity introduction and residual stress during forming process, but it also faces the challenges of surface quality[35–38]. The differences in parameters, such as laser spot size, layer thickness, and energy input, can cause the material to experience varying thermal gradients and cooling rates, ultimately influencing the microstructure and performance characteristics of the fabricated parts. Among them, laser-based techniques have emerged as the most widely adopted approach, owing to their superior precision, adaptable processing capabilities, and wide range of compatible materials[39]. These processes typically employ a layer thickness of 20 – 100 μm and complete the part fabrication through a layer-by-layer forming approach[40].

The significant challenges associated with conventional processing of refractory metals, namely their prohibitive material costs and inherent fabrication difficulties, have positioned them as an immature application area for AM. AM technique offers a transformative solution by enabling near-net-shape fabrication, thus minimizing material waste, and by allowing the formation of complex geometries that are unachievable by traditional methods.

In this review, the current states of research on AM of major refractory metals were discussed, focusing on the process-microstructure-property relationships of W, Ta, Mo, and Nb. It should be noted that Re is not discussed in this research, as its extremely high cost restricts the research width and depth.

2 Crack Formation Mechanism and Microstructure-Property Control of AM-Prepared W Parts

The extremely high melting point of W renders it a suitable candidate for applications under extreme thermal conditions. Nevertheless, the intrinsic properties of its bcc crystal structure severely constrain the processibility of W. Factors, such as low grain boundary cohesive energy and high dislocation migration activation energy, result in significant brittle characteristics at room temperature, which is manifested as high DBTT (200 – 400 °C) and low plastic deformation capability[41–44]. Furthermore, the combined effect of lattice defects, impurity segregation (gathering of oxygen, nitrogen, and carbon at the interfaces between grains), and pore structures is prone to the occurrence of intergranular fracture and crack propagation[45–47]. These factors jointly restrict the application of traditional processing methods, such as powder metallurgy[48] and hot isostatic pressing (HIP)[49], in forming complex structures.

2.1 AM formability optimization: from powder engineering to process window exploration

Laser-based AM techniques (L-PBF and L-DED) offer a new pathway to address the aforementioned key processing bottlenecks. Microstructure analysis of L-PBF-prepared parts reveals that as-deposited pure W exhibits a typical single-phase bcc structure, and its grains show preferential growth along the building direction[50–51]. The texture orientation can be precisely controlled by adjusting the process parameters. Sidambe et al[52] observed that the <111> crystallographic orientation developed along the building direction with the texture becoming increasingly distinct at higher energy densities. In contrast, Gu et al[53] observed a <100> texture when employing a zigzag scanning approach, whereas the application of a remelting technique led to the formation of a more pronounced <111> texture. However, Wang et al[54] reported differently. The random crystallographic texture obtained from an interlayer with 67° to scan direction was attributed to the influence of the process parameter. Therefore, through the precise control of texture, it is possible to enhance the mechanical properties of tungsten components in specific directions. However, this control must be combined with defect suppression (especially cracking) to fully realize its application potential, which represents a core challenge in current research.

Table 1[51,53–65] summarizes the main process parameters and development trends for fabricating pure W via L-PBF process. In Table 1, laser power is indicated by P, scanning speed is indicated by V, layer thickness is indicated by t, and scan line spacing is indicated by d. Compared with conventional manufacturing method, AM technique can refine grains and reduce porosity through localized rapid cooling, thereby offering the potential to overcome the application restrictions caused by the room-temperature brittleness of W materials. This groundbreaking advancement is expected to broaden the application scope of W in manufacturing intricate functional components, such as micro-heat exchangers and porous radiation shielding elements, thereby providing new paths for integrating structural and functional uses.

Research shows great potential but also key technical bottlenecks of the laser-based AM of W materials. Zhang et al[55] pioneered the fabrication of nanocrystalline W using L-PBF, but the used polyhedral powder led to severe metallurgical defects. This study clearly demonstrated that the shape of the raw powder plays a crucial role in determining the quality of the manufacturing process. To address this issue, Wang et al[54] compared the performance differences between polyhedral and spherical powders in L-PBF process. It is confirmed that using spherical powder enables the formation of stable and continuous molten tracks, effectively avoiding the pores and cracks, as shown in Fig. 2. The underlying reason lies in the comprehensive optimization of powder characteristics: spheroidization treatment significantly improves the powder flowability (from 15 s/50 g to 6 s/50 g) and tap density (from 5.39 g/cm^3 to 11.0 g/cm^3). Besides, the in-situ measurement results revealed that the enhanced diffusion reflection and multiple scattering effects between spherical particles substantially increased the laser absorptivity from 50% to 68%, promoting the complete melting. Ultimately, based on this powder optimization, pure

Table 1 Key process parameters in L-PBF preparation of W materials and corresponding underlying causes of cracking[51,53–65]

Key scanning parameter	Crack behavior	Material characteristic and environment
P=180–200 W; *V*=25–75 mm/s; *t*=50–70 μm; *d*=50–100 μm	Microcrack	Polygonal powder of 75 μm in size; Ar
P=400 W; *t*=30 μm; *d*=100 μm; zigzag scan; rotation at 67°	Microcrack	Ar with oxygen content below 0.01vol%
P=90 W; *V*=200–1400 mm/s; *t*=30 μm; *d*=15, 30 μm	Crack	Polygonal powder of 30 μm in size
P=400 W; *t*=30 μm; *d*=100 μm; zigzag scan; rotation at 67°	Crack on laser scanning path	Spherical powder of 28 μm in size; Ar with oxygen content below 0.01vol%
P=200–370 W; *V*=100–400 mm/s; *t*=20 μm; zigzag scan; rotation at 67°	Microcrack	Spherical powder; preheating at 50 °C; Ar with oxygen content below 0.1vol%
Rotation at 90° and 67°	Crack reduction	Spherical powder; substrate preheating at 400 °C
P=400 W; *t*=30 μm; *d*=100 μm; rotation at 67°	Crack reduction of 80%	Spherical powder of 28 μm in size with Ta addition; Ar with oxygen content below 0.01vol%
P=250–450 W; *V*=200–500 mm/s; *t*=80 μm; *d*=50 μm	Transverse crack	Spherical powder of 5–25 μm in size; preheating at 200 °C; Ar
P=200–350 W; *V*=200–400 mm/s; *t*=20 μm; *d*=50 μm; chessboard scan; rotation at 67°	Microcrack	Spherical powder; preheating at 200 °C; Ar with oxygen content below 0.01vol%
P=375, 400W; *V*=210, 330, 510, 840 mm/s; *t*=40 μm; *d*=80 μm; rotation at 90°	Microcrack	Spherical powder of 15–45 μm in size; preheating at 600, 800, and 1000 °C; Ar
P=300 W; *V*=300 mm/s; *t*=20 μm; *d*=50 μm; chessboard scan, zigzag scan, and remelting scan; rotation at 67°	Crack reduction	Spherical powder of 5–25 μm in size
P=150–300 W; *V*=200–800 mm/s; *t*=20 μm; rotation at 67°	Intergranular crack	Spherical powder with D_{50}=15.8 μm
P=400 W; *V*=100–700 mm/s; *t*=30 μm; *d*=100–120 μm; zigzag scan; rotation at 67°	Crack reduction using HIP	Spherical powder of 32 μm in size; Ar with oxygen content below 0.05vol%
P=400 W; *V*=300–700 mm/s; *t*=30 μm; *d*=50 μm; bidirectional scan; rotation at 67°	No crack	Spherical powder with D_{50}=31±2 μm; N_2

W blocks with densification of 96.0% were achieved. This breakthrough not only confirmed the decisive role of spherical powder in suppressing defects and enhancing densification, but also revealed the intrinsic powder-process-defect relationship. Further research should focus on the quantitative relationship between process parameters and fabrication quality. By introducing the key parameter of linear energy density (LED), process optimization can be guided more effectively. According to Ref. [58], a clear processing window exists: when LED (η) is within the range of 0.500–1.000 J/mm, good fabrication results can be achieved. When η reaches 0.667 J/mm, the optimal forming quality is achieved, and the relative density can reach 98.50% of the theoretical density. Guo et al[61] investigated the effect of laser power and scanning speed on the scan track characteristics, and they suggested that the optimal LED for L-PBF W parts should be less than 1.75 J/mm. Fig. 3 shows that as the linear energy increases, the width and penetration depth increase, while the height and contact angle decrease. This leads to an improvement in density to a certain extent. However, when the linear energy exceeds 1.75 J/mm, transverse cracks appear with a maximum temperature of 4630.27 °C and a cooling rate of 8.6×10^6 °C/s, indicating a threshold for defect formation.

2.2 Crack suppression strategies and mechanisms: alloying, substrate preheating, and impurity effects

Research to solve the cracking problem commonly focuses on alloying and substrate preheating. Iveković et al[59] confirmed that alloying, such as the addition of Ta, can effectively reduce cracking. However, the study also pointed out that the substrate preheating at 400 °C is insufficient to prevent cracking in pure W and W-Ta alloys due to impurities. For example, the oxygen impurity can increase DBTT of materials, thereby counteracting the toughness enhancement effect from moderate-temperature preheating. Besides, higher preheating temperatures are required to overcome cracking induced by large thermal stresses. In contrast, Müeller et al[62] employed the substrate preheating, which significantly reduced microcracks. Wang et al[60] found a high concentration of nanoscale pores enriched at the grain boundaries and proposed a nanopore-induced cracking mechanism. In the high-temperature melt pool during laser melting process, oxygen impurities in the feedstock powder react with W to form gaseous W oxides (WO_x). Since the melting point of W is much higher than the boiling point of W oxides (approximately 1700–1800 °C), the gaseous W oxides form bubbles during the solidification of W. These bubbles are

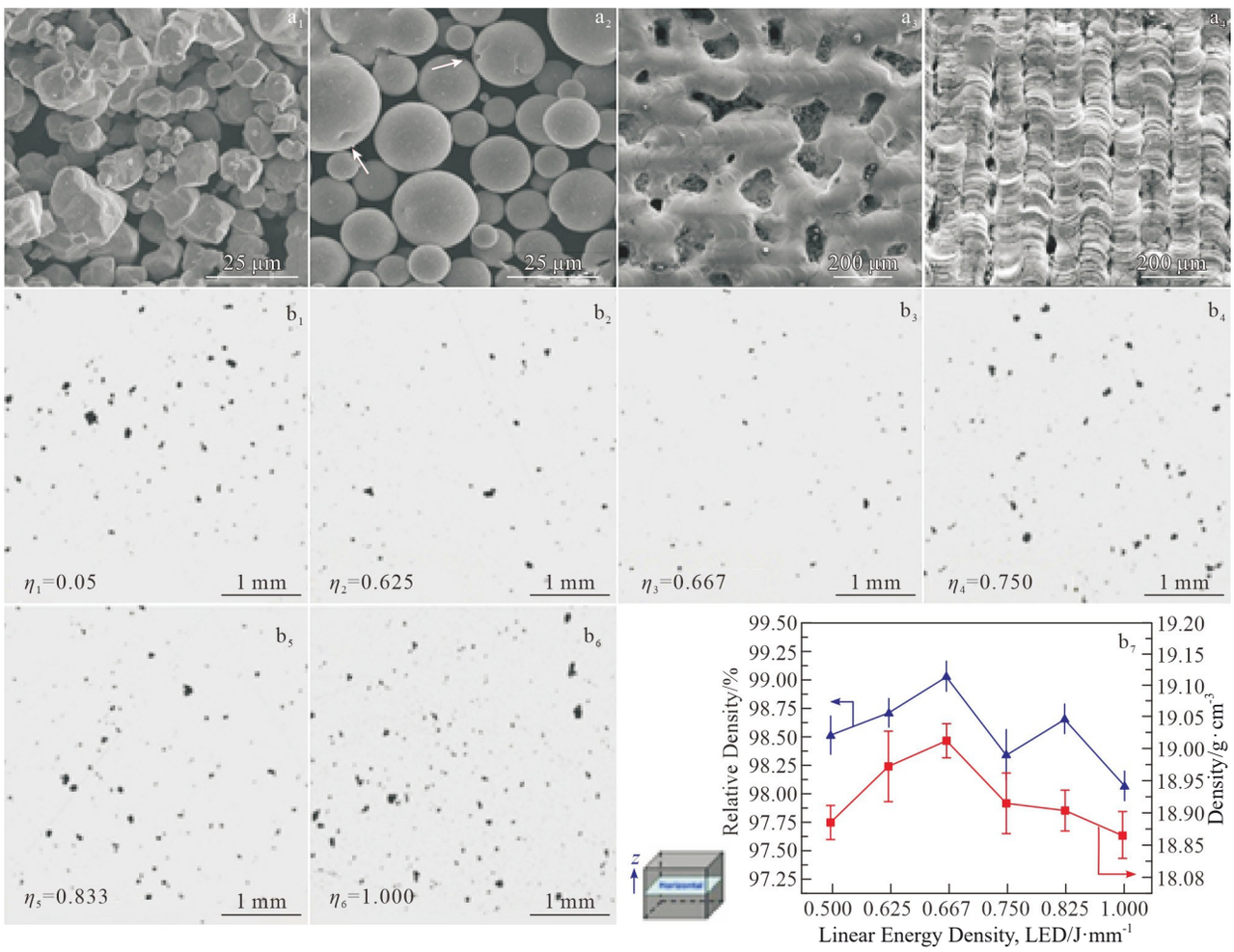

Fig.2 Microstructure control of AM-prepared W materials through raw material selection (a_1–a_4)[54] and process parameter optimization (b_1–b_7)[58]: (a_1) polyhedral W powder; (a_2) spherical W powder; (a_3) top surface morphology of AM-prepared part using polyhedral W powder; (a_4) top surface morphology of AM-prepared part using spherical W powder; (b_1–b_6) microstructures of AM-prepared W parts under different conditions; (b_7) relationship between density and LED of L-PBF-prepared W components

squeezed and aggregated at the solidifying grain boundaries, forming nanopores that severely weaken the grain boundary strength and become sources for crack initiation. Under the action of large residual stresses, the cracks appear along the weakened grain boundaries. Furthermore, it is also pointed out that adding Ta to pure W can significantly reduce cracking, as shown in Fig.4a_1–4a_6. Fig.4b_1–4b_4 show electron channeling contrast imaging (ECCI) results of pure W and W-6Ta materials. It is revealed that only a small number of nanopores are located inside the grains in pure W and W-6Ta materials, and the nanopores are trapped within the cellular walls inside the grains. The proposed sub-micrometer cellular structure in the W-6Ta alloy suppresses cracking through two synergistic mechanisms: the trapping effect that captures nanopores to reduce crack sources and the toughening effect that increases resistance against crack propagation by enhancing both strength and plasticity. Fig.4c_1–4c_2 present schematic diagrams of nanopore generation in W and W-6Ta alloys, respectively. Braun et al[66] provides a foundational framework for understanding crack formation in L-PBF-processed pure Mo and W materials. The interplay among thermal gradients, residual stress fields, and intrinsic brittleness of these materials was investigated. The research showed that during the processing of Mo and W materials, oxygen is segregated at the grain boundaries in the form of oxides, thereby forming a low-melting-point eutectic phase, which induces the generation of hot cracks. In addition, the presence of oxygen impurities can also weaken the grain boundary strength and increase DBTT of the material, thus adversely affecting the overall mechanical properties of the materials. When the material is subjected to large thermal stresses during the rapid cooling process, because the grain boundaries are weakened and the temperature is below DBTT, the stress cannot be released through plastic deformation, thus inducing cold cracks. The resulting crack network arises from the combined effects of thermal expansion and contraction.

Recently, Ramakrishnan et al[65] fabricated crack-free W samples via L-PBF under N_2 atmosphere. The introduction of

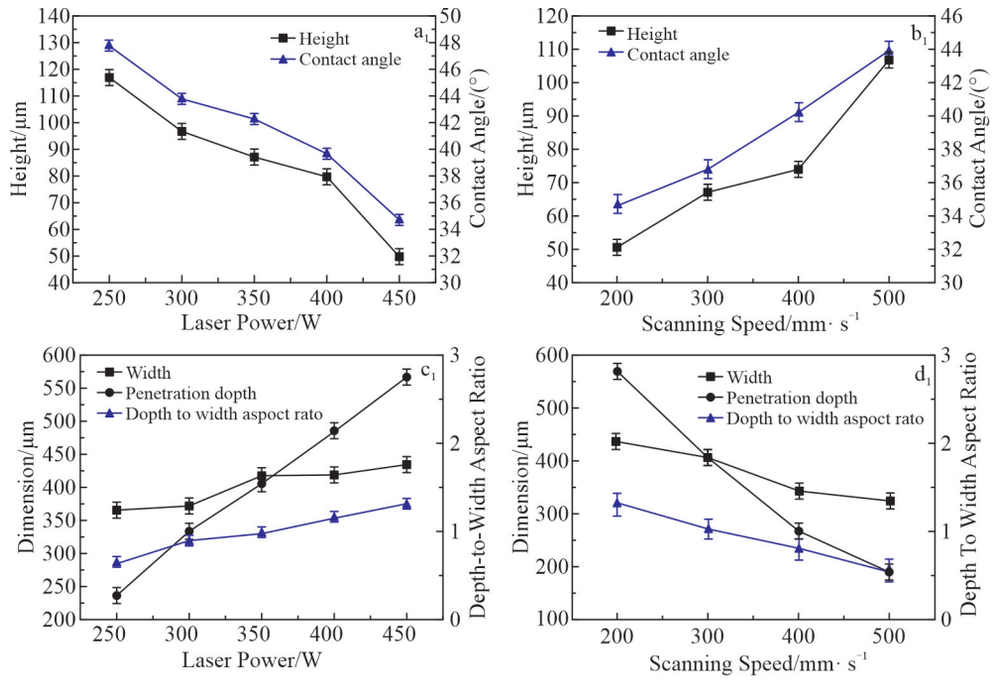

Fig.3 Influence of laser power (a_1–a_2) and scanning speed (b_1–b_2) on height and contact angle of cross-sectional scanning trajectories (a_1, b_1) as well as width, penetration depth, and depth-to-width aspect ratio (a_2, b_2)[61]

N in W materials can inhibit the oxygen diffusion, thereby reducing the oxide content at grain boundaries and ultimately enhancing the bonding strength of grain boundaries. This results in the elimination of the cracks formed unavoidably in L-PBF processing of W. Fig. 5 shows morphologies of pure tungsten samples prepared under different atmospheres[65].

2.3 Regulatory mechanism of scan strategy on microstructure and defects

Xiong et al[63] employed L-PBF remelting technique, which resulted in significant grain refinement. After remelting, the average grain size decreased from 29 μm to 14 μm. This study suggested that this was because the heat flow during the remelting process induced liquid convection into the melt pool, and the mechanisms involved the partial melting and restructuring of columnar grains to form free grains that serve as nuclei for the fine-grained zone and the higher cooling rate in the remelted zone (compared to the initial melting). Gu et al[53] studied the effects of chessboard, zigzag, and remelting scan strategies on the surface morphology, microstructure, mechanical properties, and grain orientation of pure W prepared by L-PBF process. As shown in Fig. 6a – 6f, the remelting scan strategy can eliminate pores and reduce cracks. In Fig.6, the reference axes are defined as the normal direction (ND, *x*), transverse direction (TD, *y*), and building direction (BD, *z*). Compared with the remelting scan strategy, the zigzag scan strategy results in a higher number of grain boundaries, potentially enhancing the material strength. Additionally, when the scan strategy changes from zigzag to remelting, the grain orientation in the transverse direction changes from <001> to <111>. Gu et al[53] also pointed out that the remelting scan strategy is an effective method to eliminate pore defects during L-PBF forming of pure tungsten, and it can significantly improve surface quality and reduce cracking. However, the heat accumulation caused by remelting leads to grain coarsening, which in turn significantly reduces the compressive strength and hardness.

Wang et al[57] found that the cracking problem in AM-prepared W parts is almost unavoidable, because of the large thermal stress generated during processing. Besides, the calculated surface temperature difference in W parts was as high as 7300 K, far exceeding the crack resistance threshold of 800 K. To address this issue, the effects of remelting and rotating scan strategies were investigated. It is found that 67°-rotation scan effectively suppresses longitudinal cracks by transforming the original parallel elongated grains into a three-dimensional interwoven structure. In contrast, although complete remelting can eliminate the original deposition structure, it ultimately failed to refine the grains due to the insufficient increase in the cooling rate. Therefore, these strategies only alter the crack morphology and cannot resolve the fundamental problem caused by the extreme temperature difference, thus failing to reduce the cracks effectively.

The apparent contradiction between grain refinement and coarsening can be resolved by considering that remelting is not a single well-defined process, but rather a process determined by the applied energy. The key variable is the volumetric energy density (VED) of the remelting process relative to that of the initial melting process, and it is defined as $E_v=P/VTD$, where P is the laser power, V is the scanning speed, T is the layer thickness, and D is the hatch spacing. The grain refinement can likely be achieved through a low-energy remelting process. Supposing that the energy input of the

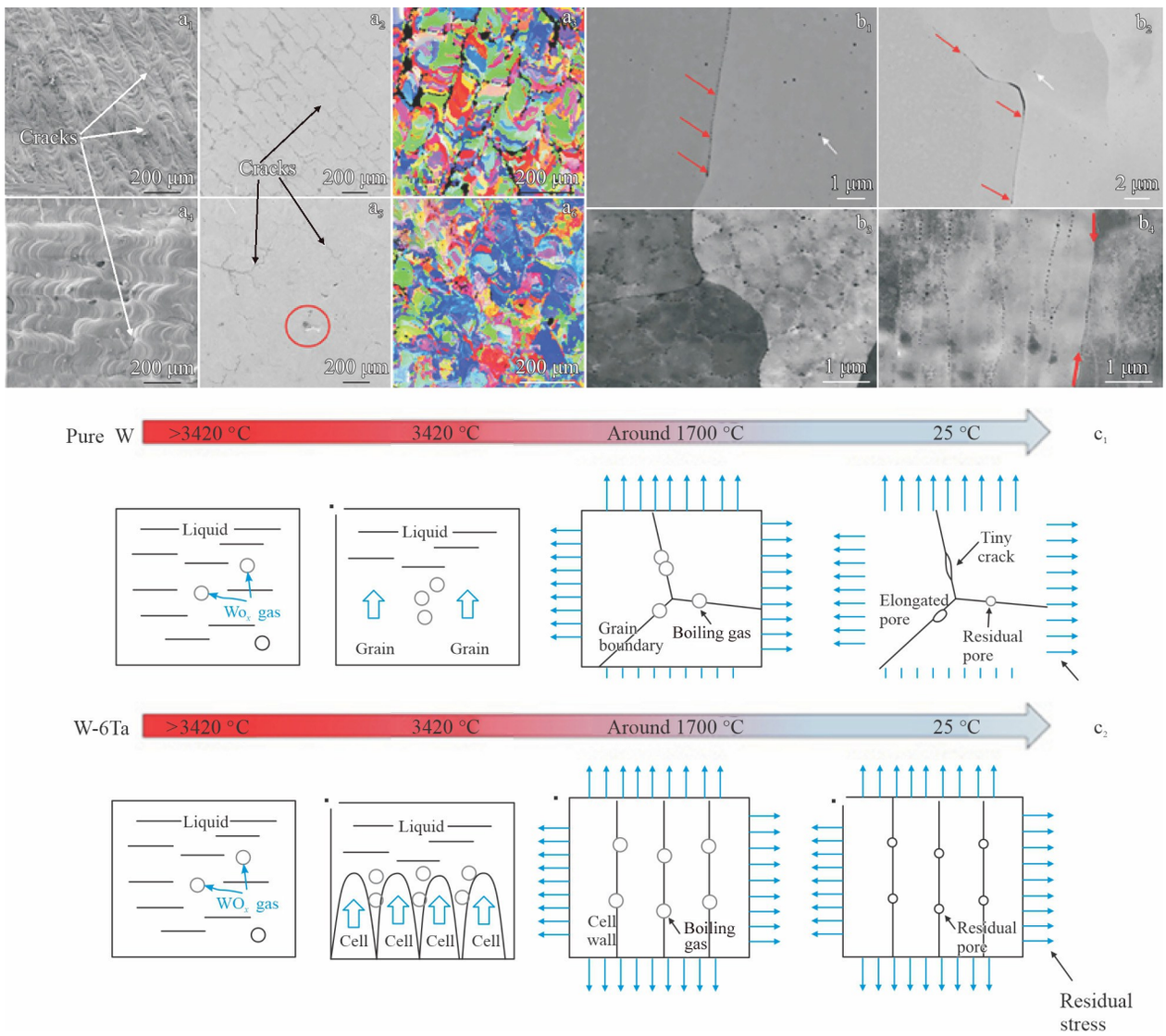

Fig.4 Original surface morphologies ($a_1 - a_2$, $a_4 - a_5$) and EBSD mappings (a_3, a_6) of pure W ($a_1 - a_3$) and W-6Ta ($a_4 - a_6$) materials; ECCI morphologies of pure W (b_1–b_2) and W-6Ta (b_3–b_4) materials; schematic diagrams of nanopore formation mechanisms in pure W (c_1) and W-6Ta (c_2) materials[60]

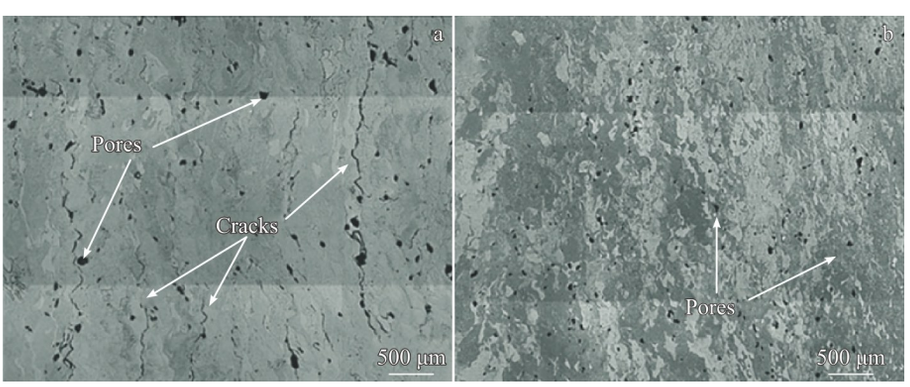

Fig.5 Morphologies of pure tungsten samples under different atmospheres[65]: (a) Ar_2; (b) N_2

second scan (achieved by increasing scanning speed, decreasing laser power, or a combination of both methods) is significantly lower than that of the first scan, a shallow melt pool can be formed. This shallow melt pool will only penetrate the top surface of the underlying solidified layer, breaking up the large columnar grains without providing

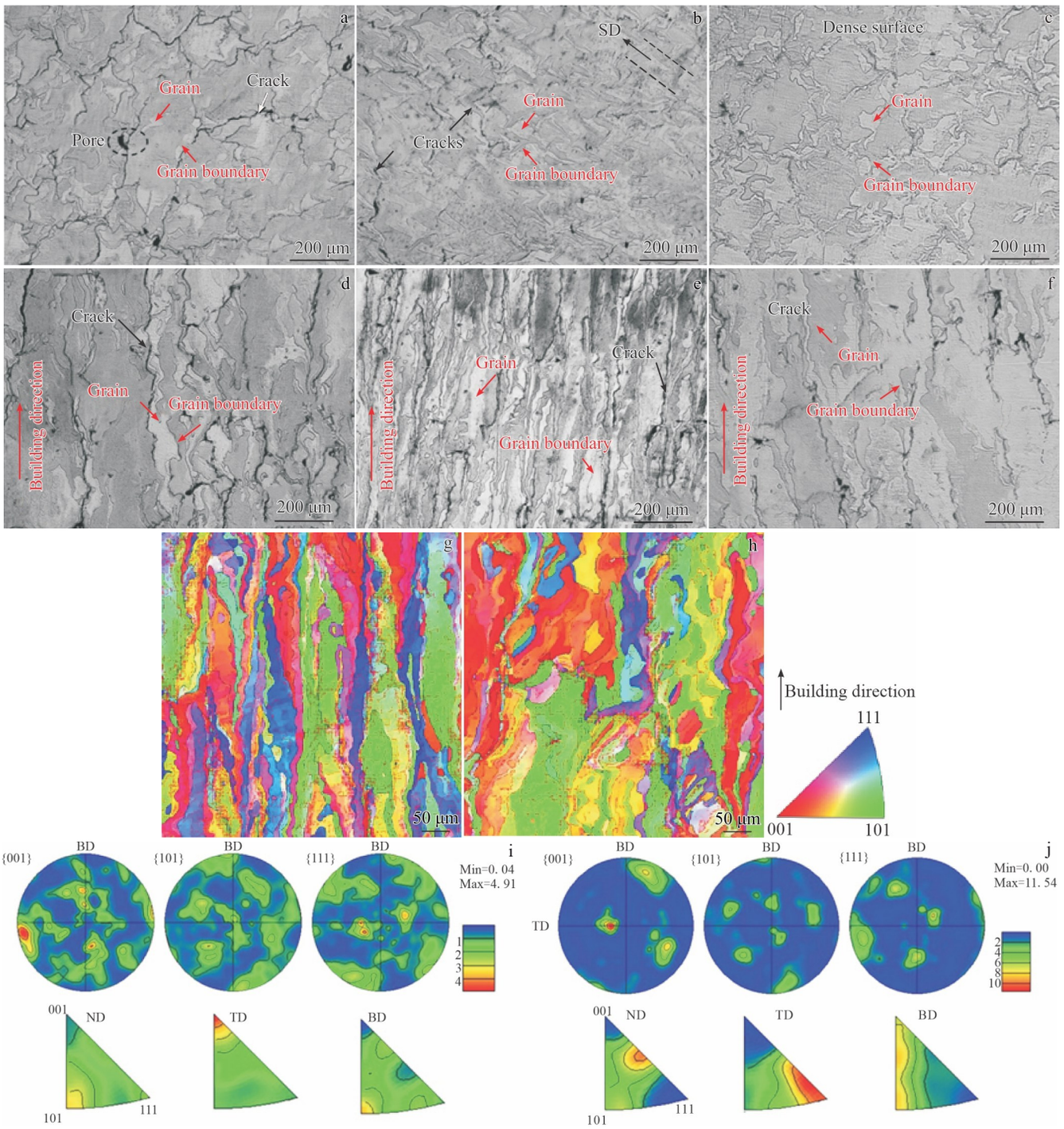

Fig.6 Morphologies (a–f), EBSD orientation maps (g–h), and pole figures coupled with inverse pole figures (i–j) of pure W prepared by L-PBF process with chessboard (a, d, i), zigzag (b, e, g, i), and remelting (c, f, h, j) scan strategies[53]

enough thermal energy to anneal the bulk material below. This process acts as a microstructure reset at the surface of each layer, promoting new nucleation and thus leading to an overall finer grain structure. Conversely, the process of grain coarsening is the result of a high-energy remelting process. If VED of the second scan is comparable to or even higher than that of the first scan, a deeper melt pool will form, transferring a significant amount of heat to the solidified material. This process is equivalent to a potent in-situ annealing or homogenization treatment. The high-temperature treatment with prolonged time provides sufficient thermodynamic driving force for grain boundary migration and the growth of larger, more stable grains, resulting in the coarsened microstructures. Therefore, the effect of remelting on grain size is not a fixed outcome but a tunable parameter. By precisely adjusting the energy input, the microstructures can be controlled through the specific requirements of the intended application.

Under the unique and complex cyclic thermo-mechanical conditions of AM, Cui et al[67] investigated the specific behavior and evolution mechanism of dislocations in W. By innovatively combining three-dimensional dislocation dynamics simulations with finite element method analysis, the complete dislocation evolution in W during L-PBF process was revealed. It is clearly demonstrated that the dynamic process of dislocation generation, motion, and annihilation is crucial for accurately predicting and controlling the mechanical properties of the final fabricated parts. The poor plasticity of AM-prepared W stems not merely from the insufficient mobility of dislocations, but from the small number of dislocations. The final dislocation density calculated from the simulation was approximately 10^{13} m^{-2}, which is significantly lower than that in the more ductile face-centered cubic metals produced by AM, such as 316L stainless steel, where dislocation densities can reach as high as 10^{14}–10^{15} m^{-2}.

3 Microstructure Regulation and Mechanical Property Optimization of AM-Prepared Ta Parts

Ta, a light-gray refractory metal, possesses significant material characteristics, including high melting point and an extremely minimal DBTT (−196 °C), and bcc crystal structure at room temperature. In recent years, owing to its remarkable high-temperature mechanical properties, good plastic workability, and outstanding biocompatibility, the application of tantalum in the aerospace, military, and biomedical fields has become increasingly widespread[68]. Particularly, in the orthopedic and dental applications, the demand for Ta has grown significantly[69].

3.1 Process feasibility and microstructure features

In the field of modern medical device manufacturing, traditional casting and powder metallurgy techniques have difficulty meeting the increasingly stringent requirements for precision and structural complexity. Particularly, in the orthopedic applications, porous Ta structures, which possess high porosity and excellent mechanical properties (flexural strength exceeding that of human cancellous bone), can provide an ideal growth environment for new bone tissue and have thus garnered significant attention[70]. However, although conventional chemical vapor deposition can be used to fabricate such scaffolds, its process complexity and high cost restrict its widespread application. To this end, L-PBF process provides an ideal solution to precisely fabricate complex porous Ta scaffolds and it has become a research hotspot in the fields of AM and clinical orthopedics[69]. Pure Ta fabricated via L-PBF process is a monophasic material with bcc structure and its microstructure exhibits distinct characteristics. The grains exhibit an elongated morphology along the building direction, resulting in a pronounced crystallographic texture[69,71–72]. Compared with the weak <100> texture obtained through traditional manufacturing methods[71], pure Ta fabricated by L-PBF process typically exhibits a pronounced <111> texture oriented along the structure direction[71,73–76], and this microstructure feature has a significant impact on its properties.

Research on the fabrication of pure Ta using L-PBF technique reveals a close correlation between process parameters and microstructure evolution. Thijs et al[69] confirmed the feasibility of fabricating pure Ta via L-PBF process. They found that the local heat input, which is controlled through the solidification direction adjustment, promotes the formation of elongated columnar grains with the <111> axis aligned with the building direction. This anisotropy originates from the synergistic effects of epitaxial growth from the melt pool, interlayer heat accumulation, and the direction of global heat flow. It is also reported that energy input is a key variable to control the crystallographic texture. Du et al[74] observed that increasing the energy input facilitates the transformation from <111> fiber texture to a more disordered texture. Meanwhile, Livescu et al[77] reported that with higher VED, the intensity of the <001> texture decreases, while the <111> texture becomes more pronounced. Oh et al[72] also found a strong <111> texture along building direction. Moreover, the texture control by scan strategy is also significant. Thijs et al[69] found that rotating the scan direction can significantly enhance texture strength. As shown in Fig.7, the sample fabricated through a 90° layer-wise rotation process (Ta90°) demonstrates the strongest texture with intensity of 4.7, which is greater than that of the non-rotated sample (Ta0°). Additionally, the volume fraction of the <111> texture in this sample reaches 93%. Without rotation, the alternating direction of heat flow caused by bidirectional scan leads to the formation of two mirror-symmetric <111> texture components. Du et al[74] achieved a columnar-to-equiaxed grain transition by adjusting the laser power (200–600 W), as shown in Fig.8, which significantly enhanced the ductility. In Fig.8, LAGB represents low angle grain boundary, and HAGB represents high angle grain boundary. These findings collectively establish a process-structure relationship model for L-PBF fabrication of pure Ta, providing a theoretical basis for the directional control of material properties.

3.2 Regulation of mechanical properties and strengthening mechanisms AM-prepared Ta parts

Research on the process optimization and property control of AM-prepared Ta alloys indicates that the fabrication quality of L-PBF and L-DED is closely associated with process parameters. The densification degree of the material generally shows a changing trend of firstly increasing and then stabilizing with the increase in energy density. Among them, the laser power and scanning speed significantly impact the densification process[74–75,77–78]. Valentino et al[78] discovered that prolonging the duration of laser exposure and using a reduced point spacing can substantially enhance the quality of interlayer bonding. Excessively fast scanning speeds can cause micropores due to Marangoni convection and the balling effect. In contrast, excessively slow speeds tend to cause pores associated with the balling effect due to melt pool overheating[79–80]. Concurrently, the characteristics of the feedstock powder play a critical role in the fabrication quality.

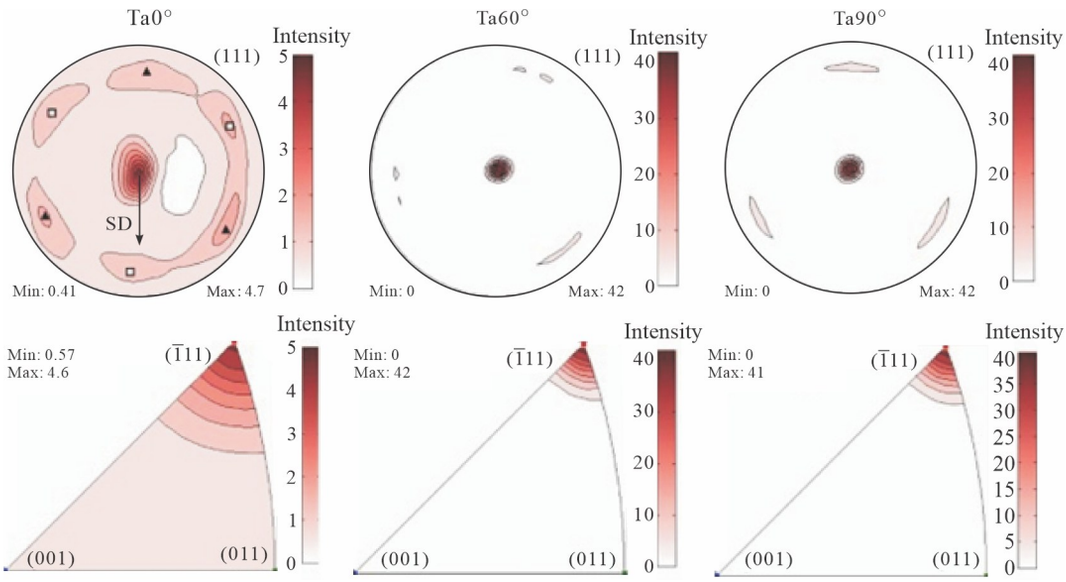

Fig.7 Texture intensity distributions influenced by different scan strategies and interlayer rotations during L-PBF process of pure tantalum[69]

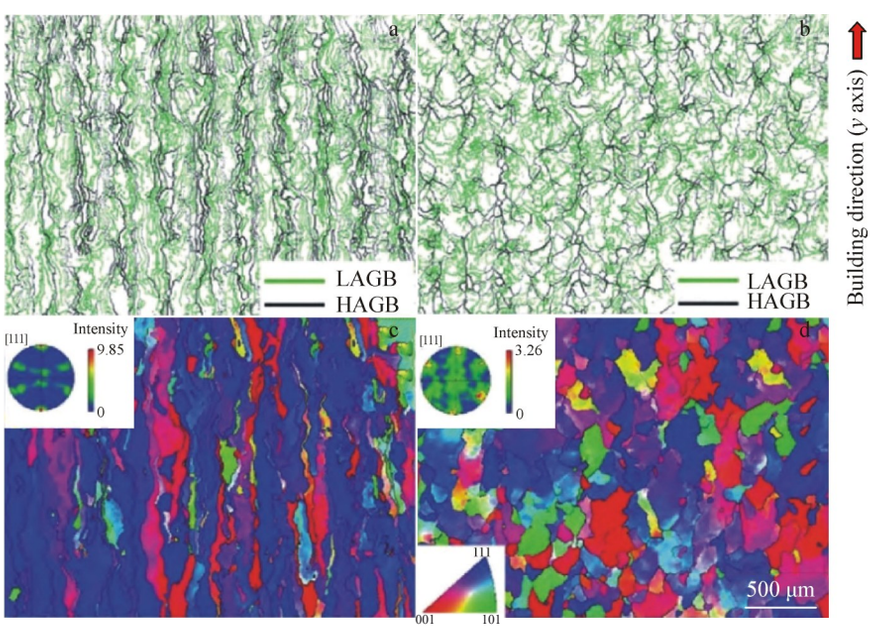

Fig.8 Grain boundary maps (a–b) and pole figures (c–d) of tantalum parts prepared by L-PBF technique at low (a, c) and high (b, d) power levels[74]

Spherical powder can achieve higher densification (98.3%), compared with non-spherical powder (97.9%) [81], and the packing density of the powder bed can be improved through powder spheroidization treatment[75,82]. Notably, the increased oxygen content resulting from powder reuse significantly reduces the material wettability, inducing balling and exacerbating porosity[73].

AM-prepared pure Ta exhibits a significantly higher hardness (150–250 HV), compared with the conventionally cast or forged counterparts (90–120 HV). This enhancement is attributed to the synergistic effects of grain refinement and residual stress[75,79–80,83–84]. Under optimized process conditions, Zhou et al[79] achieved an ultra-high hardness of 445 HV through parameter optimization, which was attributed to fine-grain strengthening and high residual stress caused by rapid laser solidification. Pure Ta fabricated by L-PBF demonstrates an ultimate tensile strength (UTS) far exceeding that of the conventionally processed counterparts and comparable to that of cold-worked material. This remarkable enhancement is a direct consequence of the high residual stresses and refined grain structure caused by AM process. Although this process can achieve a high UTS of 739 MPa, the fracture elongation is only 2%. Huang et al[85] prepared a material with UTS of 682 MPa and elongation of 26%. It is confirmed that pore

defects preferentially serve as crack initiation sites. Therefore, low porosity is a key to achieve a balance between strength and ductility[80,83]. After optimizing the process parameters, low porosity can facilitate both high strength and good ductility. Retaining the tensile properties remains a key challenge for AM-prepared pure Ta materials. Song et al[80] reported a Ta material with remarkable performance (UTS of 706 MPa and elongation of 33%), as shown in Fig. 9a. Such results are highly dependent on the process control. Generally, the fracture elongation is particularly sensitive to residual pores[75], leading to the discrepancies across different experiments. For example, Lian et al[83] reported a significantly lower ductility of 16% with UTS of 640 MPa for the as-fabricated part. Then, post-processing, such as annealing, was introduced to improve the elongation to 32% at the expense of strength. Additionally, Zhou et al[81] designed a rational triple heat treatment process and significantly improved the ductility of L-PBF-fabricated pure Ta without sacrificing strength. By transforming the microstructure from detrimental columnar grains to favorable equiaxed grains while preserving the ultra-fine cellular substructure, an excellent combination of strength (>750 MPa) and ductility (approximately 12%) was achieved. During tensile test, the continuous occurrence of short-range dislocation collapse and dislocation slip significantly increased the tensile elongation. The high tensile strength was primarily attributed to the ultra-fine cellular structure, dislocation entanglement, and the formation of hcp phase during the tensile test, as illustrated in Fig.9b. Fig. 10[85] shows microstructures observed by scanning transmission electron microscope (STEM) coupled with selected area electron diffraction (SAED) pattern and element distributions obtained by energy dispersive spectrometer (EDS).

In addition to static mechanical properties, AM-prepared Ta has also achieved significant breakthroughs in its performance under dynamic loading. Recently, Huang et al[85] reported that pure Ta samples fabricated by L-PBF (OP-Ta) exhibit excellent fatigue performance: fatigue limit as high as 348 MPa at 10^6 cycles. The fatigue strength of AM-prepared pure Ta presents a dramatic improvement over that of conventional commercial grades (CP-Ta), exhibiting enhancements of approximately 80% and 50% relative to its annealed and cold-worked counterparts, respectively. Such a significant rise in performance underscores the profound capability of AM to prepare materials with superior service reliability. More importantly, the microstructure, as the main cause of this excellent fatigue resistance, is analyzed, as shown in Fig. 10: an ultra-fine dislocation cell structure with an average size of about 300 nm, which is induced by the unique thermal process of L-PBF. This fine substructure not only provides an efficient strengthening effect but also effectively accommodates plastic deformation during cyclic loading through various mechanisms, such as dislocation penetration and cross-slip, thereby achieving a synergistic enhancement of strength and toughness. This finding provides a new approach to design refractory metals with high fatigue performance by controlling the substructure.

3.3 Effect of interstitial impurities and applications in biomedical field

Oxygen impurity acts as a critical detriment to the ductility of AM-prepared pure Ta, but its control offers a direct pathway to enhance the performance. The profound impact of oxygen content is illustrated in Ref. [82]. It is demonstrated that reducing oxygen content from 0.1422vol% to 0.0149vol% resulted in a nearly nine-fold increase in elongation from 4% (brittle) to 35% (ductile). This enhancement is underpinned by a shift in fracture mechanism towards ductile failure, which is a characteristic observed in parts fabricated from low-oxygen spherical powders with superior tensile strength. Consequently, the strict control of feedstock powder purity is not merely a recommendation but a fundamental prerequisite for achieving high-performance, damage-tolerant AM-prepared Ta components. Guan et al[86] confirmed that the ductility of the samples is closely related to the interstitial atom content. When the total content of O and N is high (approximately of 0.1200vol%), the samples exhibited brittleness. Additionally, interstitial elements, such as oxygen and nitrogen, exhibit a more complex, dual role on the mechanical properties through their distinct origins and strengthening effects. Lian et al[83] clarified that while oxygen contamination is primarily inherited from the feedstock powder, nitrogen impurities are predominantly absorbed from the processing atmosphere. Both elements contribute significantly to solid-solution strengthening in solid solution process, leading to

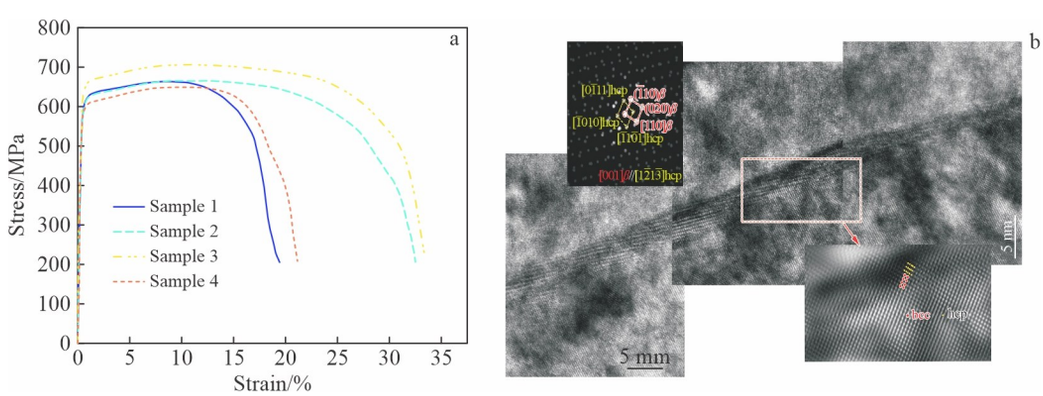

Fig.9 Tensile properties of pure Ta prepared by L-PBF[80] (a); phase interface of pure Ta prepared by L-PBF subjected to 10% tensile strain[81] (b)

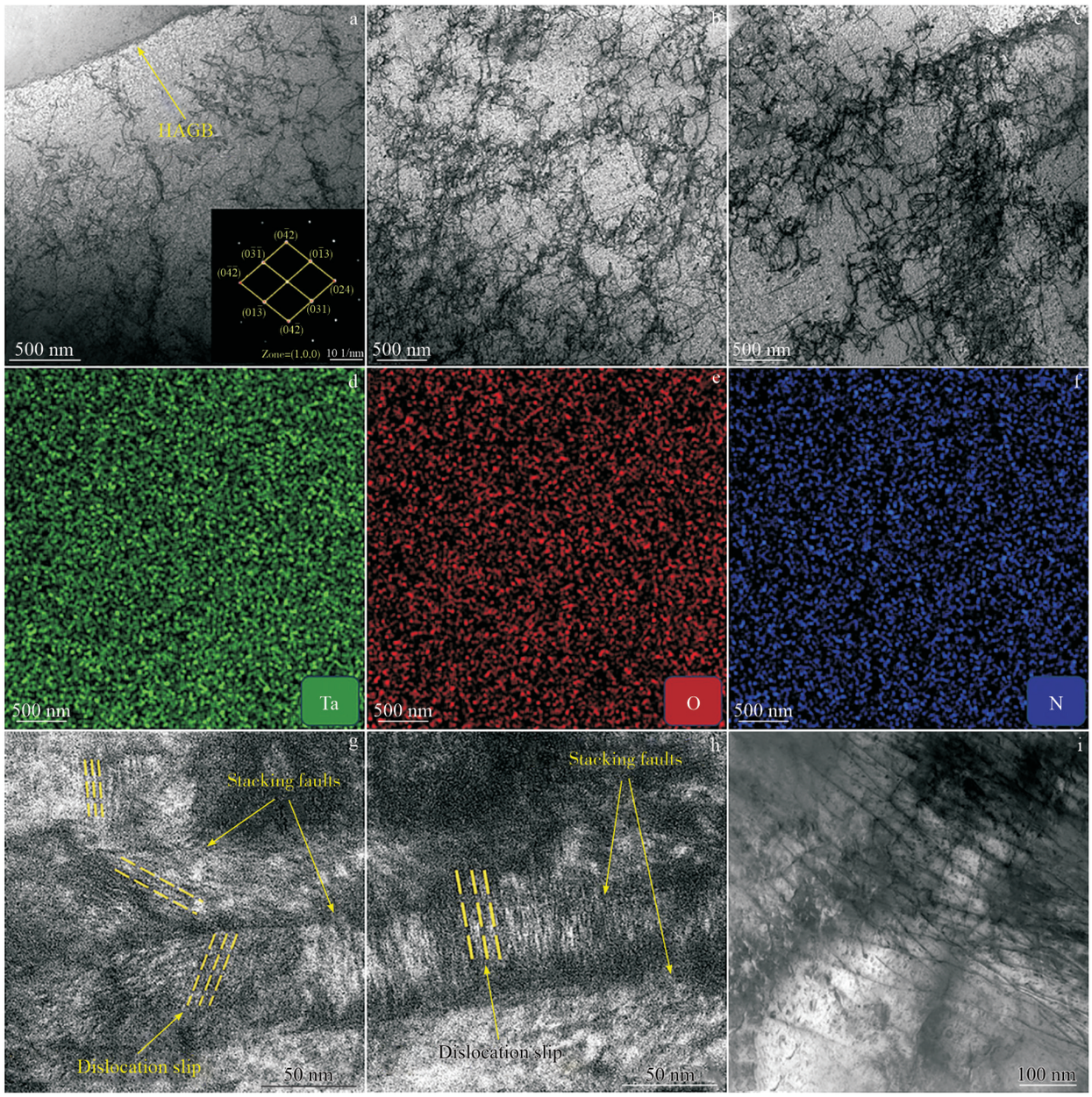

Fig.10 Microstructures near fatigue fracture region[85]: (a) bright-field STEM image and corresponding SAED pattern showing dislocations aggregating at HAGBs; (b) bright-field STEM image of networks formed by entangled aggregation of dislocations; (c) bright-field STEM image showing dislocations breaking through to the interior of networks in a region of large plastic deformation; (d–f) EDS element distributions corresponding to Fig. 10c; (g–h) TEM images of stacking faults and dislocation slips; (i) bright-field STEM image of dislocation slips

increased microhardness and tensile strength[73]. However, this strengthening effect comes at a steep price. It is also revealed that even a modest increase in oxygen from 0.0150vol% to 0.0550vol% initiates a transition from ductile failure to cleavage-assisted fracture, inferring the onset of severe embrittlement. This delicate balance is further complicated by processing parameters. For instance, Lian et al[83] demonstrated that increasing VED from 190 J/mm^3 to 310 J/mm^3 can promote the in-part oxygen pickup, raising its content to over 0.0500vol% . This phenomenon reduces the ductility and promotes the oxygen segregation at grain boundaries, triggering the catastrophic intergranular fracture, even when the material strength continues to rise. This result highlights a critical process-property trade-off, where increasing strength will irresistibly introduce failure mechanisms that degrade the material structural integrity.

In the field of medical implant applications, AM technique exhibits unique advantages. Guo et al[87] fabricated porous Ta scaffolds (porosity of 69.0%–77.8%) with controllable elastic modulus using EB-PBF process, and their compressive strength is increased with the decrease in porosity. Yang et al[88] found that the scaffolds fabricated by L-PBF possess a

superior crystal structure compared with those prepared by chemical vapor deposition. It is reported that an equiaxed fine-grained microstructure can effectively improve the ductility and biocompatibility of medical-grade Ta[74]. Combined with the precise control over complex structures afforded by L-PBF technique, the equiaxed fine-grained microstructure can provide an innovative solution for the fabrication of customized bone implants[89]. It has already demonstrated significant technical advantages in the medical field, particularly showing broad prospects in meeting special requirements, such as porous structures and biocompatibility.

4 Defect Mitigation Strategies and Mechanical Behavior of AM-Prepared Mo Parts

The relentless demand for materials capable of withstanding extreme thermal and mechanical environments in aerospace, electronics, and energy applications places refractory metals, such as Mo, at the forefront of engineering innovation. Mo has exceptional combination of high-temperature strength, stiffness, and thermal stability. However, for a long period, this potential of Mo has not been fully realized due to the substantial challenges that traditional manufacturing processes encounter in shaping this high-performance yet extremely difficult-to-machine material. Consequently, powder metallurgy has emerged as the primary method for producing Mo components. This process typically encompasses steps, such as compaction, high-temperature sintering, and subsequent thermomechanical processing, including rolling or forging. Although this method can effectively produce billets with simple geometries, such as plates and rods, it is unsuitable to fabricate high-performance components with complex three-dimensional configurations, such as internal cooling channels, lattice structures, or topologically optimized designs, therefore greatly restricting the application of Mo and its alloys.

AM techniques, particularly L-PBF, provide a revolutionary solution to overcome the aforementioned bottlenecks. However, the physical properties of Mo also present unique challenges for AM process. Mo has bcc crystal structure and high DBTT from −40 °C to 40 °C, making it extremely sensitive to the large thermal stresses and rapid cooling rates during L-PBF process, and thereby rendering it highly susceptible to defects, such as cracking[90–92]. Therefore, how to overcome the intrinsic brittleness of Mo and achieve the dense, crack-free fabrication of complex components is a critical problem that urgently needs to be solved in the current field of AM.

4.1 Defect formation mechanisms and process optimization of AM-prepared Mo parts

In L-PBF and L-DED processes, pure Mo typically exhibits a columnar grain structure growing along the building direction. Although these grains span multiple cladding layers, they benefit interlayer bonding. Inferior wettability of melt pool caused by high surface tension leads to a significant balling effect[92–93]. Rebesan et al[93] found that when Mo powder was stored in the 0.0800vol% oxygen environment, nanoscale MoO_2 precipitates (size<200 nm) formed at the grain boundaries. As shown in Fig. 11a, this oxygen segregation phenomenon directly resulted in a continuous crack network during subsequent processing[66]. Oxygen segregation is evident on the fracture surface, as shown in Fig. 11b–11c. In Ref. [94], oxygen content increased and Mo oxides formed in L-PBF-fabricated pure Mo when 3% hydrogen was added to the argon shielding gas. This result inhibited grain growth, thereby leading to a finer microstructure.

The relationship between energy density and final part density follows a non-monotonic trend, defining a clear

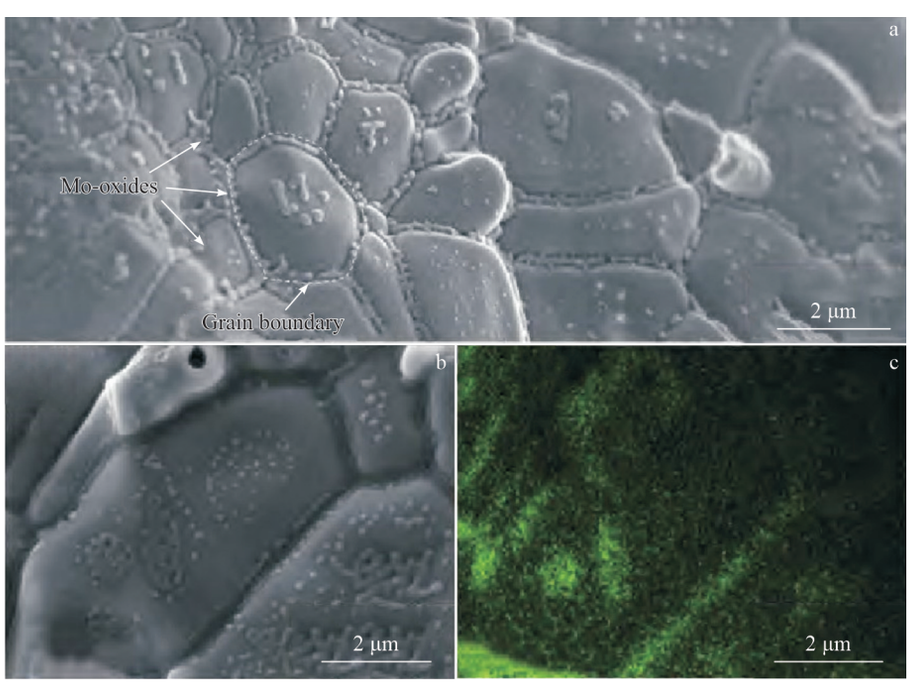

Fig.11 Fracture morphology (a), oxide morphology (b), and corresponding oxygen element distribution (c) of Mo sample prepared by L-PBF[66]

processing window. Increasing the energy input initially promotes better powder melting and reduces porosity, thus leading to higher densification. This trend continues until the density approaches a maximum value (near full density), beyond which excessive energy input becomes detrimental, causing defects to reduce the overall density[95–96]. Higashi et al[97] pointed out that porosity is closely related to VED. As VED increases, porosity significantly decreases. When VED exceeds 150 J/mm^3, nearly fully dense samples with porosity below 1% can be obtained. This analysis also identifies the scanning speed as the principal parameter that directly governs crystallographic texture evolution. Slow speeds favor the formation of <110> texture, whereas fast speeds favor the <001> texture. Other parameters (power, layer thickness) indirectly regulate the texture strength by changing VED. According to Ref. [98], when the volumetric energy density (E_v) is controlled within the range of 250 – 280 J/mm^3, the relative density of small-sized cubic samples can exceed 99.7%. The addition of La_2O_3 also has a significant effect on the reduction of porosity and cracks. After HIP treatment, the relative density of large-sized samples with added La_2O_3 reached a maximum of 99.6%. Powder morphology has a decisive influence on densification: polyhedral powder can only lead to 84% of theoretical density, while the spherical powder can increase the density to 96%–99%[92–93,95]. Faidel et al[99] pointed out that an excessive hatch spacing (30 μm) has disadvantage effect on fabrication quality, leading to heat accumulation and defects. Simply reducing the scanning speed not only fails to improve densification but actually proves counterproductive by increasing heat conduction loss. To achieve higher densification, future research should focus on increasing laser power or using thinner powder layers, rather than merely adjusting the scanning speed.

4.2 Advanced suppression strategies and their impact on mechanical properties

Overcoming crack formation remains the central challenge in AM preparation of Mo. These cracks typically manifest in three distinct and mechanism-driven morphologies: longitudinal cracks propagating parallel to the scanning direction, transverse cracks forming between adjacent melt tracks, and 45° oblique cracks often associated with maximum shear stress planes[66,92,95]. Wang et al[95] employed a 67° interlayer rotation strategy, which reduced crack length and connectivity, as shown in Fig. 12. The 67° rotation strategy is shown to be the most effective in minimizing crack defects. This is achieved by balancing the residual stress state and preventing localized stress accumulation during fabrication. By designing an ingenious heat-insulating support structure, as shown in Fig. 13a$_1$, it can control heat dissipation during the printing process, maintaining the part at higher temperatures and thus completely avoiding crack formation. Yan et al[92] also found that using a support structure to design a low-density support can have a heat preservation effect, slowing down the cooling rate of the sample, reducing thermal stress, and thereby effectively suppressing cracks and balling, as shown in Fig. 13b$_1$ – 13b$_2$. In contrast, Rebesan et al[93] attempted to reduce cracks by designing special support structures and adjusting the hatch spacing. Still, the effects are not significant, as shown in Fig. 13c$_1$–13c$_4$. Ramakrishnan et al[96] employed an N_2 shielding atmosphere and fabricated crack-free Mo components by increasing the oxygen diffusion barrier through nitrogen atom solid solution.

The mechanical properties exhibit significant anisotropy: samples tested in the vertical direction have higher strength than those tested in the horizontal direction[93]. The hardness of Mo samples reached a maximum value over 260 HV[92], which is 30%–37% higher than that of Mo prepared by conventional powder metallurgy (160–180 HV)[93]. Yan et al[92] also pointed out that Mo material produced by AM technique exhibits brittle fracture characteristics with a bending strength of 280±52 MPa and an intergranular fracture morphology. Compared with the standard Mo rod made by conventional processes (forging, grinding, and annealing), Rebesan et al[93] found that all AM-prepared samples showed significantly lower YS, UTS, and elongation at break. The standard Mo rod had an average UTS of approximately 695 MPa and an elongation at break of about 11.3%. AM-prepared samples had an average UTS of approximately 350 MPa (reduction of about 45%) and an elongation at break of only 0.53% (reduction of about 95%). Leclercq et al[100] fabricated crack-free Mo samples with ultimate compressive strength (UCS) of 510 MPa and YS of 340 MPa. They exhibited good performance in high-temperature compression tests, showing mechanical strength comparable to that of Mo manufactured

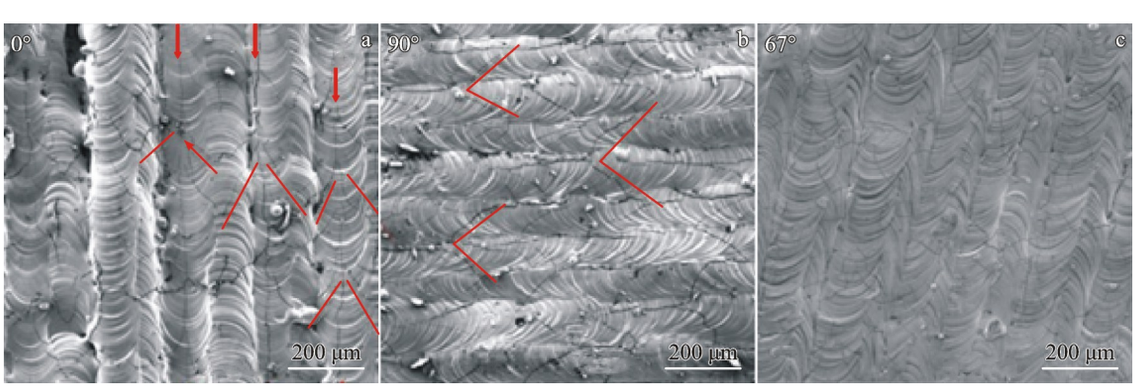

Fig.12 Microstructures of cracking in samples built with 0° (a), 90° (b), and 67° (c) rotation between layers[95]

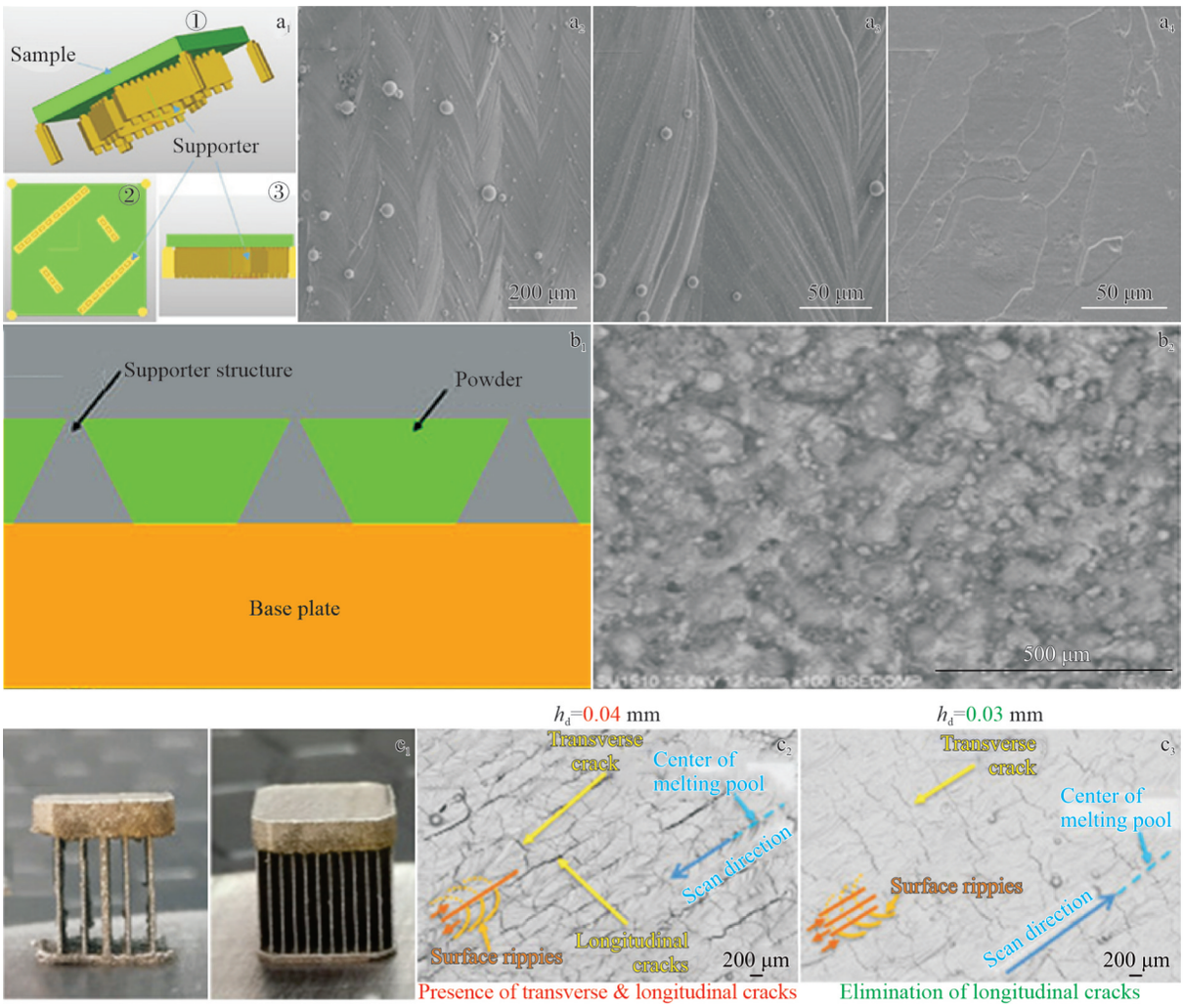

Fig.13 Schematic diagram of supporting structures (a_1) and corresponding crack-free SEM images ($a_2 – a_4$) [95]; morphology of supporting structure (b_1) and upper surface morphology of Mo samples after adding supports (b_2)[92]; specially designed supports for experiments (c_1) and corresponding microstructures with cracks (c_2–c_3)[93]

by conventional powder metallurgy process. At 800 °C, UCS was 260 MPa; at 1000 °C, UCS was 150 MPa. The strain at maximum load (δ) was 11%. The elongation at high temperatures was significantly improved, confirming the temperature sensitivity of DBTT[101].

5 Performance Optimization and Strengthening Mechanisms via Interstitial Elements of AM-Prepared Nb Parts

Nb is a refractory metal with excellent properties. Its core advantage lies in its excellent mechanical properties over a wide temperature range: its DBTT is as low as − 160 °C, which enables it to possess both outstanding high-temperature strength and low-temperature toughness[102–103]. Combined with its good thermal conductivity and processability, Nb plays an indispensable role in cutting-edge fields, such as aerospace (rocket engines, satellites), biomedical applications (implants), and high-energy physics (superconducting radio-frequency cavities) [102–104]. However, fully harnessing these excellent properties is impeded by a dual challenge rooted in both intrinsic material behavior and extrinsic processing restrictions. Intrinsically, the high-temperature chemical reactivity of materials promotes the formation of detrimental low-melting-point oxides. Additionally, conventional manufacturing techniques struggle with the economic and technical inefficiencies of fabricating complex and precise components from such materials. How to leverage its strengths while overcoming the challenges of processing and manufacturing is the fundamental issue in current niobium materials research.

5.1 AM process optimization and densification behavior

L-PBF technique offers a new pathway for the complex fabrication of Nb, but its microstructure is significantly affected by process parameters. Research has found that excessively low energy density leads to insufficient powder melting and the formation of pores, whereas excessively high energy density induces violent Marangoni convection, which, in turn, causes the formation of new pores and a slight decrease in densification, as shown in Fig.14[105]. By adjusting the energy density through varying laser power and scanning

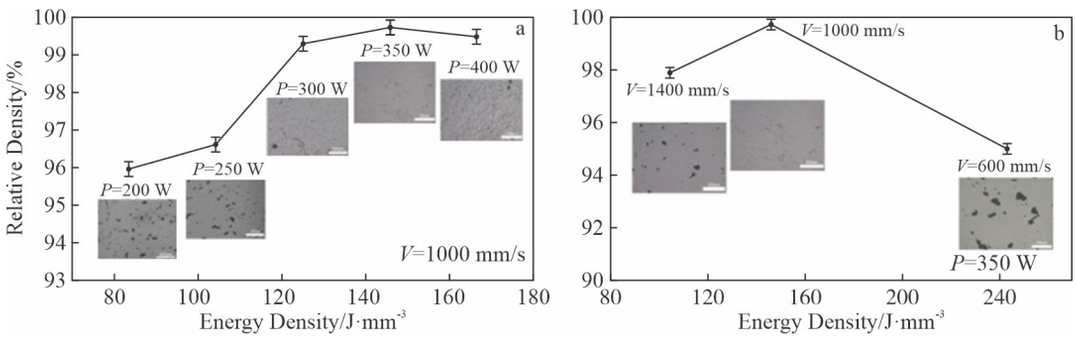

Fig.14 Comparison of Nb densification behavior as a function of energy density[105]: (a) influence of laser power at a fixed speed; (b) influence of scanning speed at a fixed power

speed, Han et al[106] identified the optimal process parameter window for fabricating defect-free high-density pure Nb samples: laser power of 330–470 W and scanning speed of 531 – 1151 mm/s. Furthermore, they pointed out that slower scanning speeds result in longer exposure of the melt pool under laser thermal energy, leading to higher contents of O and N impurities, which increase the material brittleness. Griemsmann et al[107] achieved Nb parts with a densification exceeding 99.9% and increased the building rate to 1.63 mm^3/s. The choice of scan strategy is also crucial, as smaller stripe widths can lead to a decrease in density[108].

5.2 Mechanical property regulation and dual effects of interstitial atom strengthening/brittleness

The mechanical properties of L-PBF-fabricated pure Nb exhibit significant fluctuations with microhardness ranging between 150–375 HV[105,107]. Terrazas et al[109] produced Nb by electron beam machining, and it had YS of 141±12 MPa, UTS of 225±11 MPa, and elongation at break of 34%±2%, which are comparable to those of forged materials. Griemsmann et al[107] prepared samples with UTS of 444–525 MPa and YS of 309–324 MPa. These values are nearly double those of conventionally forged or electron-beam-melted Nb materials, which is speculated to be related to the oxygen content in the powder and the elongated grain structure formed by the process.

Liu et al[105] illustrates a critical processing window for achieving optimal mechanical properties of L-PBF-fabricated pure Nb. Initially, increasing energy input enhances both

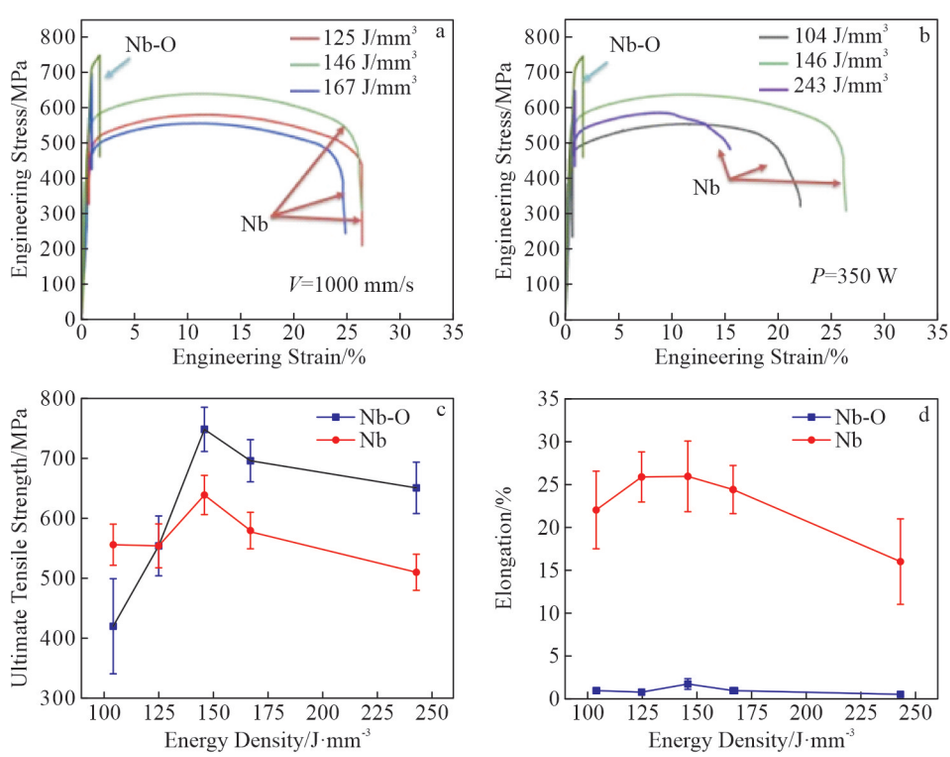

Fig.15 Correlation of mechanical characteristics of pure Nb subjected to varying degrees of oxygen contamination and under different L-PBF processing conditions[105]: (a) engineering stress-engineering strain curves under constant scanning speed; (b) engineering stress-engineering strain curves under constant laser power; (c) UTS-energy density curves; (d) elongation-energy density curves

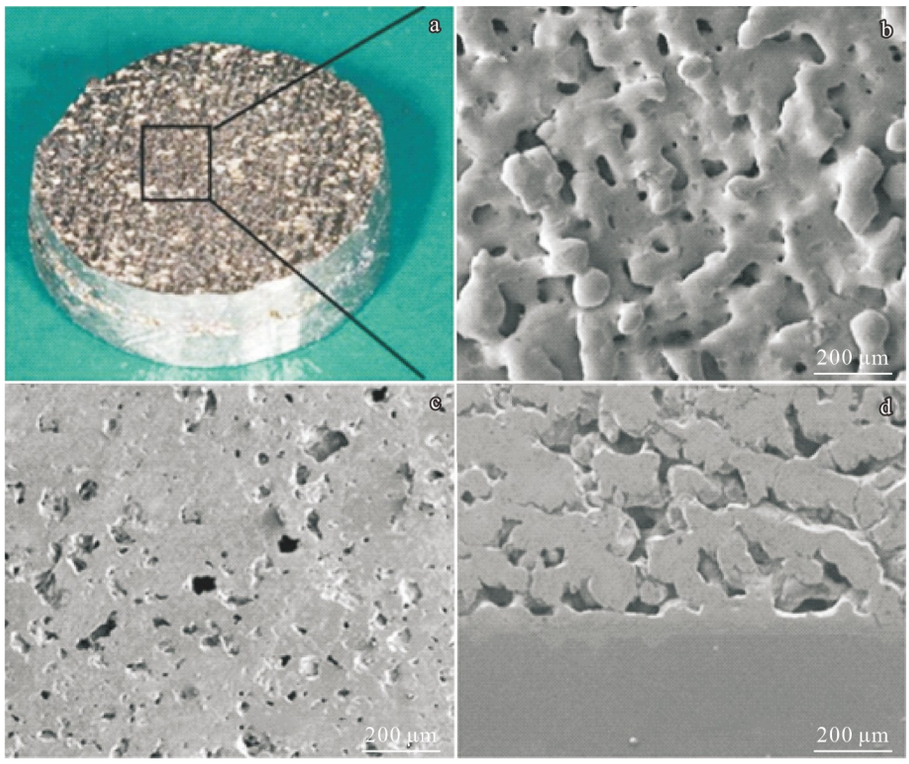

Fig.16 Appearance (a) and SEM images (b–d) of Nb coating on Ti surface[111]: (b) surface morphology of porous Nb coating; (c) cross-section morphology of porous Nb coating; (d) vertical section of both porous Nb coating and underlying Ti substrate

strength and elongation by promoting material densification. However, exceeding the optimal energy threshold triggers detrimental effects, such as intensified balling and large porosity, leading to a sharp decline in both strength and ductility. As shown in Fig. 15, a sample fabricated under optimal process parameters (146 J/mm^3) exhibited excellent comprehensive mechanical properties, owing to the presence of a large number of LAGBs (over 70%) and a high dislocation density. Its YS, UTS, and elongation was 553 MPa, 639 MPa, and 26%, respectively. This high strength is primarily attributed to fine-grain strengthening effect (average grain size of approximately 70 μm) and dislocation strengthening effect. The study also quantified the strength-ductility trade-off associated with oxygen content in Nb. An increase in oxygen can enhance the strength but severely degrade the ductility, reducing the fracture elongation from 26% to less than 2%. This embrittlement mechanism is due to the repulsive force exerted by interstitially dissolved oxygen atoms on dislocations, which impedes dislocation motion and substantially increases the energy barrier required for dislocation migration, thereby leading to a drastic deterioration in plasticity.

Chesetti et al[110] found that through theoretical calculations, the contribution of interstitial solid solution strengthening caused by oxygen and nitrogen to the strength is of the same order of magnitude as that of dislocation and subgrain boundary strengthening. This result indicates that in Nb manufactured by L-PBF process, interstitial atoms, such as dislocations, are important strengthening sources. Additionally, Fig.16 illustrates a method to prepare porous pure Nb coating on a titanium (Ti) substrate. The porous pure Nb coating on the Ti substrate achieved a microhardness of 293 HV and exhibited better biocompatibility than the substrate material, but its practical application requires further validation[111].

6 Conclusions

1) In extreme environment applications, refractory metals, such as W, Ta, Mo, and Nb, exhibit excellent high-temperature properties. However, their high melting points and intrinsic brittleness pose significant challenges to conventional manufacturing processes. AM offers a promising solution to fabricate the complex geometries and tailor the material properties. Nevertheless, practical implementation is still hindered by critical issues, such as residual stress accumulation and crack formation. Recent studies indicate that various process optimization strategies can significantly enhance forming quality and suppress defect formation. These strategies include scan strategy optimization, substrate preheating to reduce thermal gradients, alloy composition design, precise energy density control, and strict oxygen content management.

2) Future research directions include the development of machine learning-based compositional optimization methods. These advanced approaches aim to simultaneously improve both strength and ductility properties through intelligent material design. Additionally, multiparameter process optimization represents another critical research direction. This

approach seeks to establish dynamic defect control mechanisms that can adapt to varying manufacturing conditions in real time. Additionally, external field-assisted technologies, such as electric fields and magnetic fields, offer novel approaches for active solidification structure design and defect suppression. However, the engineering application of these technologies faces substantial challenges, such as the high cost of specialized equipment and high purity powders, difficulties in controlling internal defects in large components, and the absence of standardized industry protocols. These factors collectively hinder the widespread adoption of refractory metal prepared by AM.

References

1 Satya P V, Baligidad R, Gokhale A A. *Aerospace Materials and Material Technologies*[M]. Singapore: Springer, 2016: 267

2 Snead L L, Hoelzer D T, Rieth M *et al*. *Structural Alloys for Nuclear Energy Applications*[M]. New York: Elsevier, 2019: 585

3 Warlimont H, Martienssen W. *Springer Handbook of Materials Data*[M]. Cham: Springer Cham, 2018

4 Shinjo J, Panwisawas C. *Additive Manufacturing*[J], 2022, 51: 102654

5 Isayev R, Dzhumaev P. *Nuclear Engineering and Design*[J], 2023, 407: 112307

6 Que Z Y, Wei Z C, Li X Y *et al*. *Journal of Materials Science & Technology*[J], 2022, 126: 203

7 DebRoy T, Wei H L, Zuback J S *et al*. *Progress in Materials Science*[J], 2018, 92: 112

8 Johnson J L, Enneti R K. *International Journal of Refractory Metals and Hard Materials*[J], 2020, 88: 105174

9 Buj-Corral I, Tejo-Otero A, Fenollosa-Artés F. *Metals*[J], 2020, 10(5): 686

10 Zhang P L, Liu X P, Lu Y L *et al*. *Applied Surface Science*[J], 2014, 311: 709

11 Feng J Y, Wei D X, Zhang P L *et al*. *Journal of Manufacturing Processes*[J], 2023, 85: 160

12 Xiao B, Jia W P, Tang H P *et al*. *Additive Manufacturing*[J], 2022, 54: 102738

13 Gradl P, Tinker D C, Park A *et al*. *Journal of Materials Engineering and Performance*[J], 2022, 31(8): 6013

14 Yang Zhenyu, Zhu Jiangqi, Yan Xingchen. *Metal World*[J], 2023(6): 16 (in Chinese)

15 Yu Y, Song J P, Bai F *et al*. *International Journal of Refractory Metals and Hard Materials*[J], 2015, 53: 98

16 Ore A, Gerónimo D, Huaman M *et al*. *Journal of International Oral Health*[J], 2021, 13(4): 331

17 Balla V K, Bose S, Davies N M *et al*. *JOM*[J], 2010, 62: 61

18 Nikishina E, Drobot D, Lebedeva E. *Russian Journal of Non-ferrous Metals*[J], 2013, 54: 446

19 Kumar P. *Journal of the Less Common Metals*[J], 1988, 139(1): 149

20 Dobrzańska-Danikiewicz A, Wolany W. *Archives of Materials Science and Engineering*[J], 2016, 82(2): 70

21 Syre R. *Handbook on the Properties of Niobium, Molybdenum, Tantalum, Tungsten and Some of Their Alloys*[M]. Paris: North Atlantic Treaty Organization, 1965

22 Lambert J B. *Refractory Metals and Alloys*[M]. Geauga: ASM International, 1990: 557

23 Savchenko I, Stankus S. *Thermophysics and Aeromechanics*[J], 2008, 15(4): 679

24 Koechlin F, Bonin B. *Superconductor Science and Technology*[J], 1996, 9(6): 453

25 Hu L, Wirth B D, Maroudas D. *Applied Physics Letters*[J], 2017, 111(8): 8650785

26 Popov V V, Grilli M L, Koptyug A *et al*. *Materials*[J], 2021, 14(4): 909

27 Sahasrabudhe H, Bose S, Bandyopadhyay A. *Advances In Laser Materials Processing*[M]. New York: Woodhead Publishing, 2018: 507

28 Milewski J O. *Additive Manufacturing Metal, the Art of the Possible*[M]. Cham: Springer Cham, 2017: 7

29 Guo B J, Cui D C, Wu Q F *et al*. *Nature Communications*[J], 2025, 16(1): 1475

30 Xie F H, Li J N, Deng S H *et al*. *Nonferrous Metals Science and Engineering*[J], 2022, 13(4): 61

31 Wen S F, Wang C, Zhou Y *et al*. *Optics & Laser Technology*[J], 2019, 116: 128

32 Liu S Y, Shin Y C. *Materials & Design*[J], 2019, 164: 107552

33 Guo D B, Wang T Q, Tang J B *et al*. *Journal of Materials Engineering and Performance*[J], 2024, 33: 12216

34 Babuska T F, Krick B A, Susan D F *et al*. *Manufacturing Letters*[J], 2021, 28: 30

35 Gui Y W, Aoyagi K, Chiba A. *Materials Science and Engineering A*[J], 2023, 864: 144595

36 Galati M, Iuliano L. *Additive Manufacturing*[J], 2018, 19: 1

37 Gui Y W, Bian H K, Aoyagi K *et al*. *Materials Letters*[J], 2022, 328: 133096

38 Karmuhilan M, Kumanan S. *Journal of Materials Engineering and Performance*[J], 2022, 31: 2583

39 Schmidt M, Merklein M, Bourell D *et al*. *CIRP Annals*[J], 2017, 66(2): 561

40 Herzog D, Seyda V, Wycisk E *et al*. *Acta Materialia*[J], 2016, 117: 371

41 Pan S H, Yao G C, Cui Y N *et al*. *Tungsten*[J], 2023, 5(1): 1

42 Wei C, Liu L C, Gu Y C *et al*. *Additive Manufacturing*[J], 2022, 50: 102574

43 Ellis E A, Sprayberry M A, Ledford C *et al*. *Journal of Nuclear Materials*[J], 2021, 555: 153041

44 Seeger A. *International Journal of Materials Research*[J], 2022, 93(8): 760

45 Bonnekoh C, Hoffmann A, Reiser J. *International Journal of Refractory Metals and Hard Materials*[J], 2018, 71: 181

46 Zhou X, Liu X H, Zhang D H *et al*. *Journal of Materials Processing Technology*[J], 2015, 222: 33

47 Liu R, Xie Z M, Hao T *et al*. *Journal of Nuclear Materials*[J], 2014, 451(1–3): 35

48 Ma J, Zhang J Z, Liu W *et al*. *Journal of Nuclear Materials*[J], 2013, 438(1–3): 199

49 Li K L, Chen J H, Zhao C C *et al*. *Tungsten*[J], 2021, 3(2): 218

50 Deprez K, Vandenberghe S, Van Audenhaege K *et al*. *Medical Physics*[J], 2013, 40: 012501

51 Guo M, Gu D D, Xi L X *et al*. *International Journal of Refractory Metals and Hard Materials*[J], 2019, 84: 105025

52 Sidambe A, Tian Y, Prangnell P *et al*. *International Journal of Refractory Metals and Hard Materials*[J], 2019, 78: 254

53 Gu D D, Guo M, Zhang H M *et al*. *International Journal of Extreme Manufacturing*[J], 2020, 2(2): 025001

54 Wang D Z, Yu C F, Zhou X *et al*. *Applied Sciences*[J], 2017, 7(4): 430

55 Zhang D Q, Cai Q Z, Liu J H. *Materials and Manufacturing Processes*[J], 2012, 27(12): 1267

56 Enneti R K, Morgan R, Atre S V. *International Journal of Refractory Metals and Hard Materials*[J], 2018, 71: 315

57 Wang D Z, Li K L, Yu C F *et al*. *Acta Metallurgica Sinica* (*English Letters*)[J], 2019, 32: 127

58 Tan C L, Zhou K S, Ma W Y *et al*. *Science and Technology of Advanced Materials*[J], 2018, 19(1): 370

59 Iveković A, Omidvari N, Vrancken B *et al*. *International Journal of Refractory Metals and Hard Materials*[J], 2018, 72: 27

60 Wang D Z, Wang Z M, Li K L *et al*. *Materials & Design*[J], 2019, 162: 384

61 Guo M, Gu D D, Xi L X *et al*. *International Journal of Refractory Metals and Hard Materials*[J], 2019, 79: 37

62 Müller A V, Schlick G, Neu R *et al*. *Nuclear Materials and Energy*[J], 2019, 19: 184

63 Xiong Z G, Zhang P P, Tan C L *et al*. *Advanced Engineering Materials*[J], 2020, 22(3): 1901352

64 Chen J H, Li K L, Wang Y F *et al*. *International Journal of Refractory Metals and Hard Materials*[J], 2020, 87: 105135

65 Ramakrishnan T, Kumar A, Kumar T S *et al*. *Advanced Functional Materials*[J], 2024, 34(12): 2309304

66 Braun J, Kaserer L, Stajkovic J *et al*. *International Journal of Refractory Metals and Hard Materials*[J], 2019, 84: 104999

67 Cui Y N, Li K L, Wang C *et al*. *Modelling and Simulation in Materials Science and Engineering*[J], 2021, 30(2): 024001

68 Li X, Zhang Z B, He P F *et al*. *Rare Metal Materials and Engineering*[J], 2023, 52(3): 1131

69 Thijs L, Sistiaga M L M, Wauthle R *et al*. *Acta Materialia*[J], 2013, 61(12): 4657

70 Zhao Pengfei. *Plasmanitriding of Tantalum Microporous Ultrathin Materials*[D]. Taiyuan: Taiyuan University of Technology, 2020 (in Chinese)

71 Jones D R, Fensin S J, Ndefru B G *et al*. *Journal of Applied Physics*[J], 2018, 124(22): 225902

72 Oh J, Ishimoto T, Nakano T. *Journal of Smart Processing*[J], 2019, 8(4): 151

73 Tan C, Shi Q, Li K F *et al*. *International Journal of Refractory Metals and Hard Materials*[J], 2023, 110: 106008

74 Du J G, Ren Y J, Zhang M M *et al*. *Materials Letters*[J], 2023, 333: 133547

75 Shi Q, Mao X H, Tan C *et al*. *Rare Metal Materials and Engineering*[J], 2020, 49(12): 4023

76 Chen W L, Yang J Z, Kong H *et al*. *Materials Science and Engineering C*[J], 2021, 130: 112461

77 Livescu V, Knapp C M, Gray G T *et al*. *Materialia*[J], 2018, 1: 15

78 Valentino G M, Banerjee A, Lark A *et al*. *Additive Manufacturing Letters*[J], 2023, 4: 100117

79 Zhou L B, Yuan T C, Li R D *et al*. *Materials Science and Engineering A*[J], 2017, 707: 443

80 Song C H, Deng Z T, Zou Z *et al*. *International Journal of Refractory Metals and Hard Materials*[J], 2022, 107: 105882

81 Zhou L B, Chen J, Li C *et al*. *Materials Science and Engineering A*[J], 2020, 785: 139352

82 Sungail C, Abid A D. *Metal Powder Report*[J], 2020, 75(1): 28

83 Lian F J, Chen L Q, Wu C G *et al*. *Materials*[J], 2023, 16(8): 3161

84 Aliyu A A A, Poungsiri K, Shinjo J *et al*. *International Journal of Refractory Metals and Hard Materials*[J], 2023, 112: 106132

85 Huang R Z, Xie H Q, Guo L *et al*. *International Journal of Fatigue*[J], 2025, 190: 108624

86 Guan B S, Xu M G, Yang X S *et al*. *International Journal of Refractory Metals and Hard Materials*[J], 2022, 103: 105773

87 Guo Y, Chen C, Wang Q B *et al*. *Transactions of Nonferrous Metals Society of China*[J], 2022, 32(9): 2922

88 Yang J Z, Jin X, Gao H R *et al*. *Materials Characterization*[J], 2020, 170: 110694

89 Guo Y, Xie K, Jiang W B *et al*. *ACS Biomaterials Science & Engineering*[J], 2018, 5(2): 1123

90 Guo M, Luan C H, Qu J F *et al*. *Materials Reports*[J], 2023, 37(S1): 348

91 Johnson J L, Palmer T. *International Journal of Refractory Metals and Hard Materials*[J], 2019, 84: 105029

92 Yan A, Atif A M, Wang X B *et al*. *Materials*[J], 2022, 15(18): 6230

93 Rebesan P, Ballan M, Bonesso M *et al*. *Additive Manufacturing*[J], 2021, 47: 102277

94 Eckley C C, Kinkade R X, Sexton B M *et al*. *JOM*[J], 2023, 75(6): 1928

95 Wang D Z, Yu C F, Ma J *et al*. *Materials & Design*[J], 2017, 129: 44

96 Ramakrishnan T, Espiritu E R, Kwon S *et al*. *International Journal of Refractory Metals and Hard Materials*[J], 2024, 119: 106555

97 Higashi M, Ozaki T. *Materials & Design*[J], 2020, 191: 108588

98 Guan B S, Yang X S, Tang J G *et al*. *International Journal of Refractory Metals and Hard Materials*[J], 2023, 112: 106123
99 Faidel D, Jonas D, Natour G *et al*. *Additive Manufacturing*[J], 2015, 8: 88
100 Leclercq A, Mouret T, Brailovski V. *Materials Science and Engineering A*[J], 2025, 929: 148004
101 Bustin M L. *Additive Manufacturing of Molybdenum for High Temperature Structural Applications*[R]. New York: USMC Committee, 2022
102 Cai Zhang. *Copper Engineering*[J], 2022(4): 73 (in Chinese)
103 Zhu Baohui, Wu Xiangdong, Wan Min *et al*. *The Chinese Journal of Nonferrous Metals*[J], 2023, 33(1): 1 (in Chinese)
104 Motschmann F, Gerard R, Gilles F. *IEEE Transactions on Applied Superconductivity*[J], 2019, 29(5): 1
105 Liu M, Zhang J Q, Chen C *et al*. *Materials Science and Engineering A*[J], 2023, 866: 144691
106 Han S J, Ha J H, Kim W R *et al*. *Materials Letters*[J], 2025, 391: 138487
107 Griemsmann T, Abel A, Hoff C *et al*. *The International Journal of Advanced Manufacturing Technology*[J], 2021, 114: 305
108 Candela S, Rebesan P, De Bortoli D *et al*. *The International Journal of Advanced Manufacturing Technology*[J], 2024, 131(9): 4469
109 Terrazas C A, Mireles J, Gaytan S M *et al*. *The International Journal of Advanced Manufacturing Technology*[J], 2016, 84: 1115
110 Chesetti A, Banerjee S, Krishna K M *et al*. *Materials Science and Engineering A*[J], 2024, 910: 146896
111 Zhang S, Cheng X, Yao Y *et al*. *Materials Science and Engineering C*[J], 2015, 53: 50

难熔金属的增材制造工艺优化与性能调控研究进展

路笃瑞[1]，宋索成[1]，卢秉恒[2,3]
(1. 西安交通大学 金属材料强度全国重点实验室，陕西 西安 710049)
(2. 国家增材制造创新中心，陕西 西安 710300)
(3. 西安交通大学 机械工程学院，陕西 西安 710049)

摘 要：难熔金属（钨、钽、钼和铌）凭借其卓越的熔点、热稳定性和耐腐蚀性，在核能与航空航天等工业领域发挥着关键作用。这类金属具有体心立方晶体结构，其滑移系数量有限且位错运动受阻，导致显著的低温脆性，给传统加工工艺带来巨大挑战。增材制造技术提供了一种创新的方法，能够无需模具生产复杂零件，显著提高了材料的使用效率。本文概述了用于生产钨、钽、钼和铌等难熔金属的增材制造技术，特别是激光粉末床熔融技术的最新进展。本综述重点关注关键工艺参数（激光功率、扫描策略和粉末特性）对材料微观结构演变、冶金缺陷形成以及机械性能的影响机制。优化粉末特性（如球形度）、实施基板预热以及制定合金化策略能够显著提高制造零件的致密度和抗裂性能。同时，严格控制氧杂质含量以及优化能量密度输入是实现难熔金属强度和延展性同步提升的关键因素。尽管增材制造技术为难熔金属的加工提供了创新解决方案，但残余应力控制、微观结构和性能各向异性以及工艺稳定性等关键问题仍需解决。这篇综述不仅为高性能难熔金属的增材制造提供了理论基础，还为其工业应用提出了前瞻性的方向。

关键词：难熔金属；增材制造；力学性能；微观结构演变；打印工艺优化

作者简介：路笃瑞，男，2000年生，硕士生，西安交通大学金属材料强度全国重点实验室，陕西 西安 710049，E-mail：ludurui24@stu.xjtu.edu.cn